Transport in Porous Media (2024) 151:743–752
https://doi.org/10.1007/s11242-024-02062-3

Capillarity-Driven Hydrate Film Formation in Geologic Carbon Storage

David E. Fukuyama[1] · **Hugh C. Daigle**[1] · **Wen Song**[1]

Received: 27 September 2023 / Accepted: 19 January 2024 / Published online: 21 February 2024

Abstract
Much of the continental margins in the world oceans provide the necessary thermodynamic conditions to store CO_2 as ice-like hydrates (CO_2·6 H_2O). While resistant to buoyant migration and leakage, the fundamental growth mechanisms that control the injection, capacity, and security of CO_2 hydrates stored in the seafloor remain unresolved. Extensive field and laboratory testing give rise to conflicting views on the kinetics and growth configurations of hydrates, where mechanistic models reconciling the formation of hydrates observed in nature remain missing. This work elucidates a fundamental pore-scale reactive transport mechanism that underpins the rate and morphology of hydrate formation. We reveal a previously unrecognized mode of hydrate formation in porous seafloor sediments, hydrate film growth via reaction-imbibition, where superhydrophilic hydrate crystallites ($\theta \sim 0°$) formed at water–CO_2 interfaces create a secondary microporous medium ($\sim$ 10 to 100 nm pores) within lithologic sediment pores ($\sim$ 10 to 100 μm pores) to promote further hydrate growth. Unlike past diffusion-controlled models, we show that spontaneous water imbibition into the hydrate micropores establishes rapidly new water–CO_2 interfaces (i.e., hydrate formation surfaces) via capillary-driven convection and is the dominant mechanism for supplying water to the hydrate formation interface.

Keywords Carbon storage · Gas hydrates · Microfluidics

1 Introduction

Secure geologic storage of supercritical carbon dioxide (CO_2), where a high-density and low-viscosity fluid is favored to maximize storage capacity and injectivity (Ringrose and Meckel 2019), is encumbered by the buoyant mobility of CO_2 fluids (Orr 2009; Shaffer

✉ Wen Song
wensong@utexas.edu

David E. Fukuyama
fukuyama@utexas.edu

Hugh C. Daigle
daigle@austin.utexas.edu

[1] Center for Subsurface Energy and the Environment, The University of Texas at Austin, Austin, TX, USA

2010; Hawkins 2004; Goldberg and Slagle 2009a; Harvey et al. 2013). A possible solution to minimize the mobility, and thus leakage potential, of sequestered CO_2 includes storage as solid ice-like hydrates ($CO_2 \cdot 6\ H_2$) (Goldberg et al. 2008; Tohidi et al. 2010). Vast regions of the ocean floor present thermodynamically favorable conditions to form stable CO_2 hydrates for direct storage in marine sediments (Kvenvolden 1993; Koide et al. 1997a, b; Rochelle et al. 2009). Likewise, stable formation of hydrates along continental margins, adjacent to deep basalt storage sites, may secure potential buoyant migrant plumes via self-sealing hydrate caps (DePaolo et al. 2021; Goldberg et al. 2008; Tohidi et al. 2010; Gauteplass et al. 2020). The ubiquity, transmissibility, and thermodynamic favorability of seabed sediments toward CO_2 hydrate formation offers potential for scalable, rapid, and secure CO_2 disposal.

Questions remain, however, on the fundamental reactive transport mechanisms of hydrate formation that underpin the injectivity, capacity, and security of CO_2 storage in the seafloor (Dai and Seol 2014; Kleinberg et al. 2003; Katagiri et al. 2017; Bhattacharjee et al. 2015). Despite extensive field and laboratory measurements, existing theories on the pore- and interfacial-level mechanisms of hydrate formation fail to reconcile field phenomena (You et al. 2019; Palodkar and Jana 2017; Kvamme 2021). Specifically, current theory predicts that upon nucleation at water–CO_2 interfaces where both reagents (i.e., water and CO_2) are plentiful, hydrates grow slowly into the water phase and is rate-limited by CO_2 dissolution into water and diffusion across the hydrate crust (You et al. 2019; Palodkar and Jana 2017; Kvamme 2021; Chaouachi et al. 2015, 2017). Models based on this theory, however, cannot explain the early losses in injectivity observed frequently in the field (Gauteplass et al. 2018; Ding and Liu 2014). To elucidate the growth mechanisms of CO_2 hydrates in seabed sediments, fundamental resolution of the pore-level hydrate growth phenomena are required.

Here, we provide microscale (~ μm), real-time (~ ms) insights into the pore-level processes underlying CO_2 hydrate formation using *operando* geochemical microfluidic visualization experiments. A geochemical microfluidic platform with representative pore geometry and surface chemistry of unconsolidated seabed sediments (hereafter "micromodel") is saturated with simulated seawater (3.5 wt.% NaCl) and injected with CO_2 at – 3°C and ~ 3 MPa to induce CO_2 hydrate growth. Pressure is controlled to form hydrates, where rapid diffusion of pressure perturbations ensures simultaneous hydrate nucleation and growth across the micromodel. All experiments are conducted under quiescent (i.e., no fluid injection) conditions. Notably, a previously unknown hydrate growth phenomenon, rapid hydrate film growths enabled by reaction-imbibition, is revealed that challenges the longstanding model for diffusion-limited hydrate growth into bulk waters.

2 Visualization of Hydrate Formation in Micromodels

Hydrate formation and dissociation experiments were performed using a high-pressure etched silicon micromodel, following the fabrication process outlined in Buchgraber et al. (2012), Song and Kovscek (2016), and Song et al. (2018). The pore geometry of the micromodel resembles a thin section of an unconsolidated sandstone, representative of marine sands present at hydrate forming conditions. The pore geometry is etched into the silicon wafer and a transparent glass plate is anodically bonded to the silicon wafer to allow direct visualization of fluid flow and transport at the μm scale. Oxidized silicon and glass hold similar wetting characteristics to quartz sands. The pore geometry and wettability of silicon

micromodels provide a close approximation of siliciclastic ocean floor sediments. The micromodel is contained in a stainless steel holder with Swagelok inlet and outlet ports, capable of maintaining the pressures necessary for hydrate formation.

To reach hydrate forming conditions, two Quizix QX Series 6000 pumps were used to maintain pressure on the inlet and outlet ends of the micromodel. The pump on the inlet supplied the system with CO_2 (Carbon dioxide, UN1013, Praxair), and the pump connected to the outlet supplied deionized water (Barnstead E-Pure Ultrapure Water Purification system at 18.2 MΩ·cm) mixed with 3.5 wt.% NaCl (Sodium chloride, 7647–14-5, ACS reagent ≥ 99.0%, Sigma-Aldrich).

At ambient pressure and room temperature (21 °C), the micromodel was fully saturated with 3.5 wt.% NaCl brine using Pump 1 (Fig. S2, Pump 1). To purge air from the system, a secondary valve (Fig. S2, V3) was opened, and a small amount of CO_2 was flushed through the system and vented to the fume hood. The system was then pressurized to 3.0 MPa using CO_2 gas with Pump 2 (Fig. S2, Pump 2). Flushing CO_2 through the system lowered water saturation to residual saturations. Pump 2 was set to a constant gas pressure at 3.0 MPa while Pump 1 was set to hold a constant volume and to monitor downstream pressure. The system was cooled to - 3 °C using a Fischer Scientific Isotemp cooling bath, with 25 vol.% Ethylene Glycol ($(CH_2OH)_2$, A11591.36, ≥98.5 %, Thermo Scientific) and 75 vol.% deionized water, which was circulated to maintain a constant temperature. After 30 min inside the cold water reservoir, hydrate formation was initiated with a small pressure pulse using Pump 2. The pressure pulse was required to perturb the system into hydrate nucleation.

All experiments were imaged using a Nikon Eclipse LVDIA-N microscope. A Nikon DS-Fi 3 (5.9 MP Color SCMOS) camera captured videos at 30 frames/second, with a resolution of 1440 x 1024, (0.5 μm/pixel). The spatial distribution of water was delineated using fluorescence microscopy. Water was dyed with 0.01 wt.% Rhodamine B ($C_{28}H_{31}ClN_2O_3$, CAS: 81–88-9, ≥95%, Sigma-Aldrich). RGB image sequences were taken using a Nikon B-2A filter (EX 450–490, DM505, B A 520). During hydrate formation, Rhodamine B is excluded from the hydrate cage structure. As a result, fluorescence signals emitted from Rhodamine B describe only the spatial distribution of water.

3 In situ Visualization of Hydrate Formation

In situ observation of hydrate formation reveals a previously unreported mode of hydrate growth, where, counter to current theory, a thin hydrate film grows rapidly away from the bulk water (Fig. 1, Movie S1). We initialize the experiments by injecting CO_2 injection into the water-saturated seabed sediment (Fig. 1A, $t = 0$). Here, bulk water is retained in the pore throats and along grain walls. Roughness is etched into the walls of the grains to retain water and to aid visualization (Fig. S1). While some water films exist on the top and bottom surfaces of the micromodel, they are thin (~ 10 nm) (Tokunaga 2012) and hold large surface area to volume ratios. Interaction between water and CO_2 molecules initiates the formation of CO_2 hydrate crusts along water–CO_2 interfaces (Fig. 1A, $t = 0.733$ s), where both water and CO_2 are plentiful.

Hydrate growth thereafter, surprisingly, is dominated by a thin hydrate film that propagates rapidly away from the bulk water and into the CO_2-occupied pore body (Fig. 1A, $t = 1.333$ to 30 s). The growth of this hydrate film is contrary to theoretical predictions, where slow, diffusion-limited growth of interfacial hydrate crusts into the bulk water (Chaouachi et al. 2015, 2017) are expected. Quantification of the micrograph

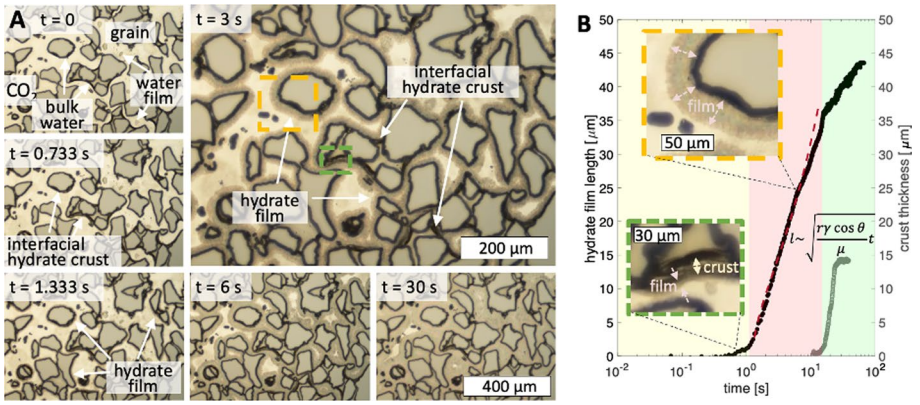

Fig. 1 A new mode of hydrate formation is revealed. **A** Thin hydrate films grow rapidly away from the bulk water, counter to conventional theory. An initial water/CO_2 system (t = 0) at 3 MPa and - 3 °C begins to form a thin hydrate crust at the water/CO_2 interface (t = 0.733 s). Shortly thereafter, thin films of hydrate propagate away from the water and into the CO_2-occupied pore body (t = 1.333 to 30 s). **B** The rate of hydrate film growth (black) far exceeds that of the diffusion-limited interfacial hydrate crust that grow into the bulk water over long times (gray circle). Scaling analysis shows that the length of the hydrate film varies with $t^{1/2}$, resembling capillary-driven flows (red dashed line)

series show that hydrate film growths dominate at early times, and scale with the square root of time, $t^{1/2}$ (Fig. 1B, black data, red dashed line). The $t^{1/2}$ scaling of the hydrate film length, l, is reminiscent of capillary-driven flows where the motion of an interface is governed by capillarity and viscous forces (Fig. 1B, red dashed line). In contrast, the diffusion-limited interfacial crust grows at a much slower pace (Fig. 1B, gray data).

The underlying mechanisms controlling this rapid hydrate film growth phenomenon are elucidated by quantifying the growth behavior of the hydrate film and the distribution of reagent components necessary to form CO_2 hydrates (i.e., water and CO_2, Fig. 2). At any time during hydrate growth, we note that the length of the hydrate film is equal across the porous micromodel in large and small sand pores (Fig. 2A, arrow sets). That is, the propagation of the hydrate film is independent of the lithologic pore that it resides within. Micrograph time-series of hydrate films propagating across the micromodel also corroborate the lithologic pore-independence of the hydrate film growth phenomenon (Fig. 2B). The consistence in hydrate film growth rates observed across large and small pores suggests that the growth phenomenon is controlled by characteristics intrinsic to the hydrate material itself rather than the lithologic pore.

A second question remains on the supply of water toward hydrate formation. Propagation of the hydrate film away from bulk water requires a transport mechanism to supply water to the reaction interface (i.e., CO_2-water interface). Time-resolved fluorescence micrograph series of water dyed with Rhodamine B (Movie S2, Fig. 2C, water is green, Rhodamine B is excluded from the hydrate crystal structure) shows changing distribution of water during hydrate growth. Here, bulk water layers surrounding the etched sand grains, not observable under bright-field microscopy, are visible under fluorescence (Fig. 2C, t = 0). With hydrate growth, water is drawn out of the bulk water (Fig. 2C, t = 1 to 50 s) and redistributed following the position of the hydrate film. Comparison between the water distribution (i.e., water film length) and hydrate film

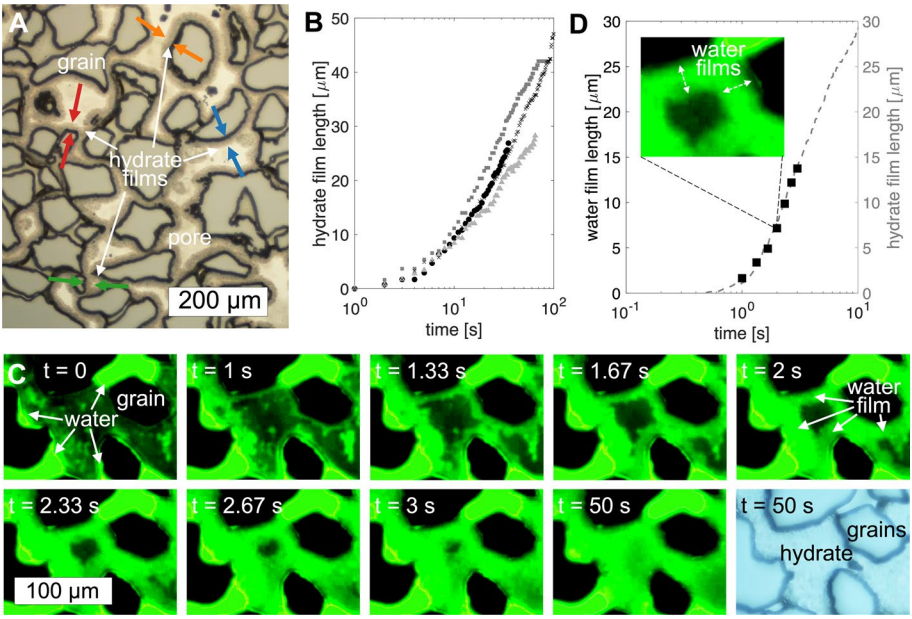

Fig. 2 Reaction imbibition growth of hydrate films driven by capillarity. **A**, **B** Hydrate films grow at the same rate, independent of the lithologic pore that they grow in. **C** Fluorescence micrographs showing water in green. Fluorescence around the sand grains (e.g., $t = 0$) indicate bulk water retained by the rough wall surfaces that are otherwise not observable under bright-field microscopy. All grains are etched with rough wall surfaces (i.e., orthogonal to the focal plane) to retain bulk water and to aid with visualization. Water is drawn out of the bulk water ($t = 1$ to 50 s) during hydrate growth. **D** Water distribution in the pore (black squares) follows that of hydrate films (gray dashed line) during hydrate growth

growths (Fig. 2D) over several experiments show that the water and hydrate films follow each other closely.

The combination of the above observations, namely rapid hydrate growth away from the bulk water scaling with $t^{1/2}$, growth rates independent of the lithologic pore occupied, and rapid redistribution of water with the hydrate film ($\sim t^{1/2}$), suggest a convectively supplied reaction-imbibition process. Here, we propose that the formation of the microporous hydrate medium (Chaouachi et al. 2015) (pore radius ~ 10 to 100 nm) imbibes water spontaneously from the residual bulk water into the hydrate film to deliver water convectively to the reaction interface. Spontaneous water imbibition driven by cornering/crevice flows in microporous media are well-documented for wetting surfaces (Song and Kovscek 2015). In the presence of CO_2, the contact angle of water on hydrates is $\theta \sim 0°$ based on

$$\cos\theta = \frac{\gamma_{H-CO_2} - \gamma_{H-water}}{\gamma_{CO_2-water}} \tag{1}$$

where the interfacial tensions γ between structure II hydrate (H), water, and CO_2 are $\gamma_{H-water} \sim 9.3$ to 30 mN/m (Gauteplass et al. 2020; Brewer et al. 1998; Zhang et al. 2012), $\gamma_{CO_2-water} \sim 30$ mN/m (Chalbaud et al. 2009), and $\gamma_{H-CO_2} \sim 60.5$ to 124.2 mN/m (Wei and Maeda 2022). Similarly, the corresponding positive spreading coefficient $S = \gamma_{H-CO_2} - (\gamma_{CO_2-water} + \gamma_{H-water}) > 0$ specifies that the energy-minimizing arrangement is one where water coats the solid CO_2 hydrate crystal entirely. The superhydrophilicity of

the < μm hydrate film pores enable spontaneous water imbibition and convective transport to the reactive CO_2-water interface.

Scaling analyses reduces the reaction-imbibition process, assuming fast hydrate formation kinetics, to a capillary-driven flow. We simplify the porous hydrate continua as a bundle of tubes with radii r ~ 20 nm, where the position of the water–CO_2 interface, l, in each tube is given by the balance between capillarity and viscous forces:

$$l^2 \sim \frac{r\gamma \cos(\theta)}{2\mu} t \tag{2}$$

with water–CO_2 interfacial tension $\gamma \sim 52$ mN/m, CO_2/water/hydrate contact angle $\theta \sim 0°$, and water viscosity $\mu \sim 1.8$ mPa·s. Promisingly, the capillary-driven interface displacements are in agreement with the measured hydrate film propagation (Fig. 1B, black data, red dashed line).

We clarify here that the water supply for hydrate film growths must originate from bulk water transported convectively via capillarity through the microporous hydrate continuum as opposed to pre-existing water films on the micromodel surface. While discrete water films that are not connected to bulk waters exist (Fig. 3A, B t = 0), they do not provide sufficient water to sustain the hydrate films observed (~ 10 nm for water film on SiO_2 in CO_2 environment

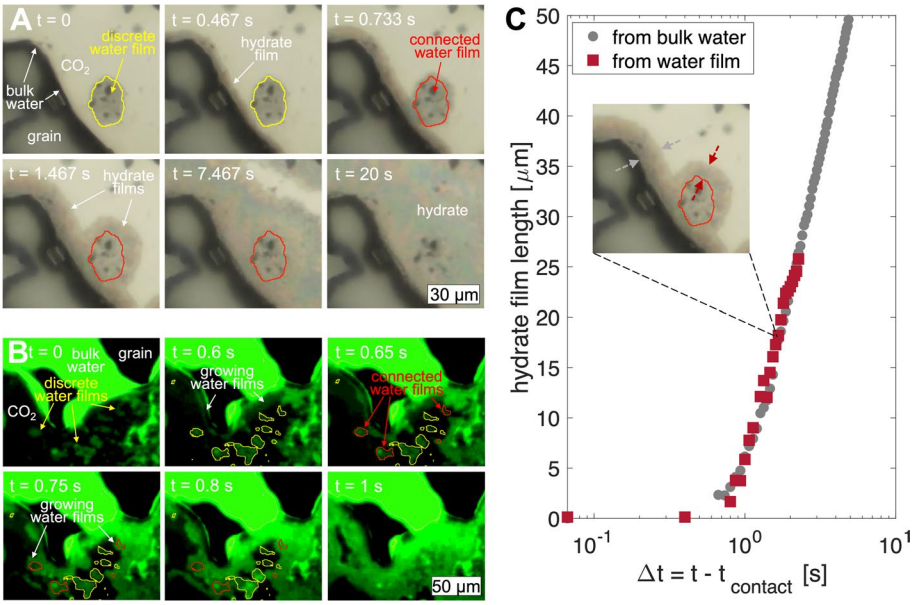

Fig. 3 Evidence that the water required for hydrate growth is supplied from spontaneous imbibition of bulk water into the porous hydrate continuum rather than from surface-bound water films. **A** An initially discrete water film (outlined in yellow) that is isolated from bulk residual pore water is tracked over time with hydrate film growth. Prior to contact with the growing hydrate film ($t < 0.7$ s), the discrete film remains constant in size, even with the formation of CO_2 hydrate. Upon contact with the growing hydrate film ($t \sim 0.7$ s, initial water film outlined in red), however, the surface-bound film forms a continuous porous medium that is connected to the bulk water from which hydrate films begin growing ($t \sim 0.733$ to 20 s). **B** Water fluorescence show, similarly, the motion of water prior to ($t < 0.65$ s) and following contact with the growing hydrate film. **C** Growth of hydrate films initiating from the bulk water (gray) and from initially discrete water films that come into contact with the bulk water during film growth (red) show similar rates when normalized to the time elapsed since contact with the bulk water source

(Tokunaga 2012)). Assuming stoichiometric consumption of water during hydrate formation (6 mol water for 1 mol of CO_2 hydrate) and hydrate density of ~ 1100 kg/m^3 leads to an upper bound of ~ 1.28 on the volume of hydrate expected per volume of water, far less than the volume of hydrate films observed (Fig. 3).

Further, bright field (Fig. 3A, Movie S3) and fluorescence (Fig. 3B, Movie S4) tracking of hydrate film and water distributions, respectively, show that that both the hydrate and discrete water films are quiescent so long as they remain discrete from the bulk water. That is, prior to contact with the bulk water (Fig. 3A, $t = 0$ to 0.467 s, Fig. 3B, $t = 0$ to 0.6 s), no growth is observed for the hydrate or water films (Fig. 3A, B, yellow outlines showing initial interfaces). Upon contact (Fig. 3A, $t > 0.733$ s, Fig. 3B, $t > 0.65$ s), when a connected pathway for capillary-driven water convection is established through the porous hydrate continuum, however, both the hydrate and water films extend past their original boundaries.

Interestingly, hydrate film growth from the discrete water film, upon contact with the bulk water, follows the same $t^{1/2}$ scaling observed for bulk hydrate films. Comparison of hydrate films propagating from the bulk water–CO_2 interfaces with those extending from the discrete water film boundaries show the same growth phenomenon when measured as a function of time after contact with the bulk water (Fig. 3C). The lack of growth prior to contact and the capillary-driven growth scaling after continuity with the bulk water confirms the minimal contribution of surface water films on the observed hydrate film growth, and the importance of the porous hydrate continuum on water transport and hydrate growth.

Below we describe the reaction-imbibition mechanism schematically to explain the hydrate film growth phenomenon (Fig. 4, side view of micromodel). As water is displaced by the injected CO_2, bulk water is trapped in the pore throats and along rough grain walls where clays and other fine materials may reside (Fig. 4A, grain with rough wall). On clean sand grains (Fig. 4A, micromodel top and bottom), discrete water films that are disconnected from the bulk water are retained. When provided thermodynamic conditions that are favorable to hydrate formation, hydrate crusts nucleate at all water–CO_2 interfaces, including bulk waters and discrete water films (Fig. 4B). In the discrete water films, nearly all of the water molecules are consumed by the hydrate crust because of their large surface area to volume ratio (water films ~ 10 nm thick (Tokunaga 2012)).

Nucleation of hydrate crystallites at water–CO_2 interfaces establishes a secondary porous medium with ~ 10 to 100 nm pores. The secondary hydrate inter-crystallite pores are ~ 3 orders of magnitude smaller than those of the lithologic pores (i.e., unconsolidated sands) with superhydrophilic surfaces ($\theta \sim 0°$) that provide an opportunity for spontaneous imbibition of water into the newly established hydrate continuum (Fig. 4C). Notably, as water imbibes into the hydrate continuum and wets the surfaces of the hydrate crystallites, a new water–CO_2 interface is established where additional hydrates form and imbibe water (Fig. 4C, inset). The continued nucleation and growth of hydrate crystallites here provide a possible explanation for previous characterizations showing log-normal crystal size distributions (Chaouachi et al. 2017). This self-propagating reaction-imbibition hydrate growth process continues until either the bulk water is consumed, or the hydrate fills the lithologic pore (Fig. 4D).

4 Conclusions

The findings here reveal a previously unreported mechanism for hydrate formation that influences the morphology and rate of CO_2 hydrate growth in sediments. Specifically, a self-propagating reaction-imbibition process, whereby porous hydrate continua deliver

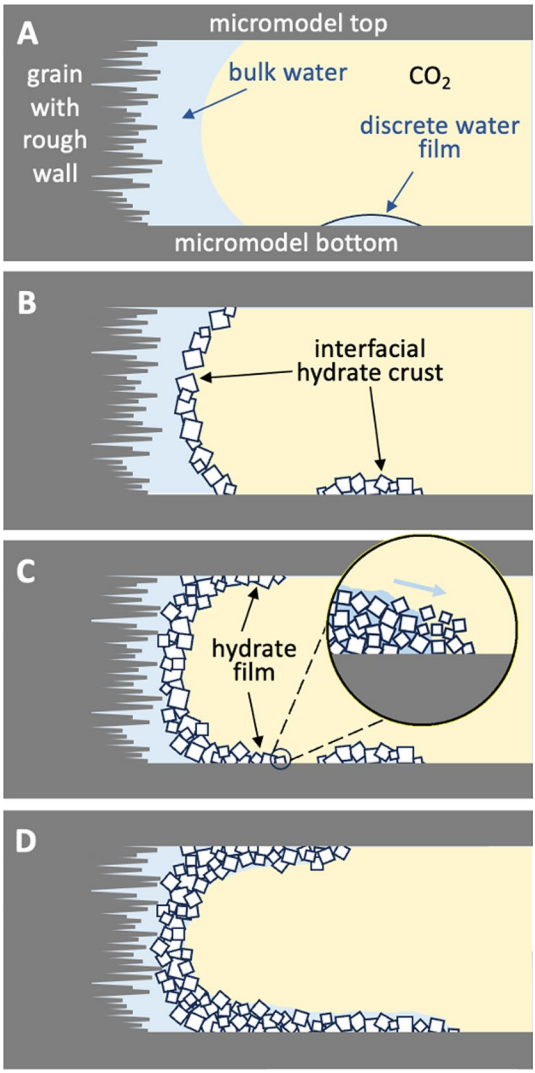

Fig. 4 Mechanistic depiction of the reaction-imbibition hydrate film growth process. **A** Side view of an initially water-saturated micromodel that is injected with CO_2. Residual pore water (i.e., bulk water) is retained in pore throats and around the rough walls of the etched grains. On smooth, water-wet surfaces (e.g., top and bottom of the micromodel), thin discrete water films are retained. **B** Immediately following CO_2 introduction, a thin hydrate crust forms at all water–CO_2 interfaces. We note that because the discrete water films hold extremely large interface-to-volume ratios (water film ~ 10 nm thick on etched silicon (Tokunaga 2012), nearly all of the water in the film is consumed to form the interfacial hydrate crust. **C** Hydrate film formation as a result of reaction-imbibition. Water-wetting ($\theta \sim 0°$) hydrate crystallites establish a secondary porous medium with ~ 10 to 100 nm pores that are ~ 3 orders of magnitude smaller than those of the unconsolidated sand pores (Goldberg and Slagle 2009b) The newly formed hydrate medium imbibes water spontaneously from the bulk water to establish a water–CO_2 interface at the growth surface of the hydrate, where additional hydrate forms. Here, water is supplied convectively to the reaction interface via capillarity, and much exceeds the rate of CO_2 diffusion through the interfacial crust. Hydrate growth from the initial discrete water film is halted because of insufficient water. **D** The self-propagating process continues until either the water is consumed or the hydrate film has filled in the pore. As the hydrate film grows into the hydrates formed by the initial discrete water films, a continuous porous hydrate medium is established and growth continues

water convectively to the CO_2-water interface via spontaneous imbibition to enable rapid hydrate formation is elucidated for the first time. Notably, the process revealed here show that hydrates act as water transport *facilitators*, in contrast to their role as diffusion-limited CO_2 transport *barriers* (You et al. 2019; Palodkar and Jana 2017) dictated by existing hydrate growth theory.

Supplementary Information The online version contains supplementary material available at https://doi.org/10.1007/s11242-024-02062-3.

Acknowledgements We would like to gratefully acknowledge Shunxiang Xia for his assistance in fabricating the micromodels used in this experiment, Geir Ersland, and Bill Waite for their helpful discussions in experimental hydrate formation, and Don DePaolo for useful discussions.

Author Contributions All authors contributed to the experimental design. DF performed the experiments. DF and WS contributed new analytical tools. All authors analyzed the data. WS and DF wrote the paper. All authors revised the manuscript.

Funding This work was supported by the Energy Institute at The University of Texas at Austin and the Laboratory Directed Research and Development (LDRD) program at Sandia National Laboratories. Sandia National Laboratories is a multimission laboratory managed and operated by National Technology and Engineering Solutions of Sandia, LLC., a wholly owned subsidiary of Honeywell International, Inc., for the U.S. Department of Energy's National Nuclear Security Administration under contract DE-NA-0003525.

Availability of data and materials The datasets generated during and analyzed during the current study are available from the corresponding author on reasonable request.

Declarations

Conflicts of interest The authors have no relevant conflicts of interests to disclose.

References

Bhattacharjee, G., Kumar, A., Sakpal, T., et al.: Carbon dioxide sequestration: influence of porous media on hydrate formation kinetics. ACS Sustain. Chem. Eng. **3**, 1205–1214 (2015)

Brewer, P.G., Orr, F.M., Friederich, G., et al.: Hydrate formation in the deep sea. In situ experiments with controlled release of methane, natural gas, and carbon dioxide. Energy Fuels **12**, 183–188 (1998)

Buchgraber, M., Kovscek, A.R., Castanier, L.M.: A study of microscale gas trapping using etched silicon micromodels. Transp. Porous Media **95**, 647–668 (2012)

Chalbaud, C., Robin, M., Lombard, J.M., et al.: Interfacial tension measurements and wettability evaluation for geological CO2 storage. Energy Procedia **32**, 98–109 (2009)

Chaouachi, M., Falenty, A., Sell, K., et al.: Microstructural evolution of gas hydrates in sedimentary matrices observed with synchrotron x-ray computed tomographic microscopy. Geochem. Geophys. Geosyst. **16**(6), 1711–1722 (2015)

Chaouachi, M., Neher, S.H., Falenty, A., et al.: Time resolved coarsening of clathrate crystals: the case of gas hydrates. Cryst. Growth Des. **17**, 1458–2472 (2017)

Dai, S., Seol, Y.: Water permeability in hydrate-bearing sediments: a pore-scale study. Geophys. Res. Lett. **41**, 4176–4184 (2014)

Ding, T., Liu, Y.: Simulations and analysis of hydrate formation during CO2 injection into cold saline aquifers. Energy Procedia **63**, 3030–3040 (2014)

Gauteplass, J., Almenningen, S., Ersland, G., et al.: Hydrate seal formation during laboratory CO2 injection in a cold aquifer. Int. J. Greenhouse Gas Control **78**, 21–26 (2018)

Gauteplass, J., Almenningen, S., Ersland, G., et al.: Multiscale investigation of CO2 hydrate self-sealing potential for carbon geo-sequestration. Chem. Eng. J. **381**, 122646 (2020)

Goldberg, D., Slagle, A.: A global assessment of deep-sea basalt sites for carbon sequestration. Energy Procedia **1**, 3675–3682 (2009)

Goldberg, D., Slagle, A.: Characterization of sand sediment by pore size distribution and permeability using proton nuclear magnetic resonance measurement. Energy Procedia **1**, 3675–3682 (2009)
Goldberg, D., Takahashi, T., Slagle, A.: Carbon dioxide sequestration in deep-sea basalt. PNAS **105**(29), 9920–9925 (2008)
Harvey, O.R., Qafoku, N.P., Cantrell, K.J., et al.: Geochemical implications of gas leakage associated with geologic CO 2 storage: a qualitative review. Environ. Sci. Technol. **47**(1), 23–36 (2013)
Hawkins, D.: No exit: thinking about leakage from geologic carbon storage sites. Energy **29**, 1571–1578 (2004)
Katagiri, J., Konno, Y., Yoneda, J., et al.: Pore-scale modeling of flow in particle packs containing grain-coating and pore-filling hydrates: verification of a Kozeny–Carman-based permeability reduction model. J. Nat. Gas Sci. **45**, 537–551 (2017)
Kleinberg, R.L., Flaum, C., Griffin, D.D., et al.: Deep sea NMR: methane hydrate growth habit in porous media and its relationship to hydraulic permeability, deposit accumulation, and submarine slope stability. J. Geophys. Res. Solid Earth **108**, 2508 (2003)
Koide, H., Shindo, Y., Tazaki, Y., et al.: Deep sub-seabed disposal of CO2: the most protective storage. Energy Convers. Manage. **1**, 3675–3682 (1997)
Koide, H., Takahashi, M., Shindo, Y., et al.: Hydrate formation in sediments in the sub-seabed disposal of CO2. Energy **22**(2–3), 279–283 (1997)
Kvamme, B.: Kinetics of hydrate formation, dissociation and reformation. Chem. Thermodyn. Thermal Anal. **1–2**, 100004 (2021)
Kvenvolden, K.: Gas hydrates-geological perspective and global change. Rev. Geophys. **31**, 171–187 (1993)
Orr, F.: Onshore geologic storage of CO2. Science **325**, 1656–1658 (2009)
Palodkar, A.V., Jana, A.K.: Formulating formation mechanism of natural gas hydrates. Sci. Rep. **7** (2017)
Ringrose, P., Meckel, T.: Maturing global CO2 storage resources on offshore continental margins to achieve 2DS emissions reductions. Sci. Rep. **9**, 1–10 (2019)
Rochelle, C., Camps, A., Long, D., et al.: Can CO2 hydrate assist in the underground storage of carbon dioxide? Geol. Soc. **319**, 171–183 (2009)
Shaffer, G.: Long-term effectiveness and consequences of carbon dioxide sequestration. Nat. Geosci. **3**, 464–467 (2010)
Song, W., Kovscek, A.R.: Functionalization of micromodels with kaolinite for investigation of low salinity oil-recovery processes. Lab Chip **15**, 3314–3325 (2015)
Song, W., Kovscek, A.R.: Direct visualization of pore-scale fines migration and formation damage during low-salinity waterflooding. J. Natl. Gas Sci. Eng. **34**, 1276–1283 (2016)
Song, W., Ogunbanwo, F., Steinsbø, M., et al.: Mechanisms of multiphase reactive flow using biogenically calcite-functionalized micromodels. Lab Chip **18**(24), 3881–3891 (2018)
Tohidi, B., Yang, J., Salehabadi, M., et al.: CO2 hydrates could provide secondary safety factor in subsurface sequestration of CO2. Environ. Sci. Technol. **44**, 1509–1514 (2010)
Tokunaga, T.: DLVO-based estimates of adsorbed water film thicknesses in geologic CO 2 reservoirs. Langmuir **28**, 8001–8009 (2012)
Wei, Y., Maeda, N.: Critical Surface Tension and Specific Surface Free Energy of Clathrate Hydrate. Energy Fuels **36**, 407–414 (2022)
You, K., Flemings, P.B., Malinverno, A., et al.: Mechanisms of Methane Hydrate Formation in Geological Systems. Rev. Geophys. **57**, 1146–1196 (2019)
Zhang, J., Di Lorenzo, M., Pan, Z.: Effect of surface energy on carbon dioxide hydrate formation. J. Phys. Chem. B **116**, 7296–7301 (2012)